NeuroImage: Clinical 21 (2019) 101657

Contents lists available at ScienceDirect

NeuroImage: Clinical

journal homepage: www.elsevier.com/locate/ynicl

Optimized preoperative motor cortex mapping in brain tumors using advanced processing of transcranial magnetic stimulation data

Laura Seynaeve[a,*,1], Tom Haeck[b,e], Markus Gramer[b,e], Frederik Maes[b,e], Steven De Vleeschouwer[c], Wim Van Paesschen[a,d]

[a] Laboratory for Epilepsy Research, KU Leuven, Herestraat 49, Box 7003, 3000 Leuven, Belgium
[b] Department ESAT-PSI, KU Leuven, Kasteelpark Arenberg 10, Box 2441, 3001 Leuven, Belgium
[c] Department of Neurosurgery, UZ Leuven, Laboratory for Experimental Neurosurgery and Neuroanatomy, Department of Neurosciences, Leuven Brain Institute, KU Leuven, Herestraat 49, Box 7003, 3000 Leuven, Belgium
[d] Department of Neurology, UZ Leuven, Belgium
[e] Medical Imaging Research Center, UZ Leuven, Herestraat 49, Box 7003, 3000 Leuven, Belgium

ARTICLE INFO

Keywords:
Transcranial magnetic stimulation
Electrical field modelling
Presurgical functional mapping
Motor cortex

ABSTRACT

Background and objective: Transcranial magnetic stimulation (TMS) is a useful technique to help localize motor function prior to neurosurgical procedures. Adequate modelling of the effect of TMS on the brain is a prerequisite to obtain reliable data.

Methods: Twelve patients were included with perirolandic tumors to undergo TMS-based motor mapping. Several models were developed to analyze the mapping data, from a projection to the nearest brain surface to motor evoked potential (MEP) amplitude informed weighted average of the induced electric fields over a multilayer detailed individual head model. The probability maps were compared with direct cortical stimulation (DCS) data in all patients for the hand and in three for the foot. The gold standard was defined as the results of the DCS sampling (with on average 8 DCS-points per surgery) extrapolated over the exposed cortex (of the tailored craniotomy), and the outcome parameters were based on the similarity of the probability maps with this gold standard.

Results: All models accurately gauge the location of the motor cortex, with point-cloud based mapping algorithms having an accuracy of 83–86%, with similarly high specificity. To delineate the whole area of the motor cortex representation, the model based on the weighted average of the induced electric fields calculated with a realistic head model performs best. The optimal single threshold to visualize the field based maps is 40% of the maximal value for the anisotropic model and 50% for the isotropic model, but dynamic thresholding adds information for clinical practice.

Conclusions: The method with which TMS mapping data are analyzed clearly affects the predicted area of the primary motor cortex representation. Realistic electric field based modelling is feasible in clinical practice and improves delineation of the motor cortex representation compared to more simple point-cloud based methods.

1. Introduction

Neurosurgical procedures in or close to the motor cortex can be complicated by permanent motor deficits. To prevent damage while aiming to maximize resection, functional mapping is required, especially in tumor surgery, where anatomy can become distorted and functional reorganization can have occurred. In functional mapping, we aim to outline the cortical motor representation (Pitkänen et al., 2017) i.e., the cortical area that is necessary and sufficient for the generation of movement, rather than only the hotspot of a specific muscle. The current gold-standard to delineate the motor cortex is direct electrical cortical stimulation (DCS). DCS is time-consuming, allows for only

Abbreviations: TMS, transcranial magnetic stimulation; MEP, motor evoked potential; DCS, direct cortical stimulation

* Corresponding author.
E-mail addresses: laura.seynaeve@uzleuven.be (L. Seynaeve), frederik.maes@kuleuven.be (F. Maes), steven.devleeschouwer@uzleuven.be (S. De Vleeschouwer), wim.vanpaesschen@uzleuven.be (W. Van Paesschen).
[1] Current address: Department of Neurology, UZ Brussel, Laarbeeklaan 101, 1090 Jette, Brussels, Belgium.

https://doi.org/10.1016/j.nicl.2019.101657
Received 20 September 2018; Received in revised form 21 December 2018; Accepted 3 January 2019
Available online 09 January 2019

limited sampling in case of tailored craniotomies and can't be used for preoperative planning or patient counselling. fMRI can help localize functions in the brain, but its use in pre-surgical planning is limited by the altered neuro-vascular coupling -especially near lesions with increased vascularization, and the fact that all regions involved in a task become active and not just the essential brain regions (Hill et al., 2000; Hou et al., 2006; Sunaert, 2006; Wang et al., 2012; Zacà et al., 2014). A non-invasive, well-tolerated brain stimulation technique able to electrically activate brain regions responsible for generating movement directly- transcranial magnetic stimulation (TMS) - seems the most promising technique for reliable functional pre-operative mapping.

TMS over perirolandic brain regions can lead to motor evoked potentials (MEPs). The resulting MEPs can be measured using electromyography (EMG). The first experiments using TMS for presurgical mapping date back to the nineties (Krings et al., 1997) but most studies were published after TMS-coils coupled to neuronavigation became commercially available. Even with neuronavigation, only the position of the coil on the scalp is defined and the accuracy of functional mapping depends on our ability to predict from the position of the coil with a diameter spanning over ten centimeters, the exact location and spread of activation in the brain. Previous studies testing TMS mapping prior to tumor surgery reduced the effect of a TMS stimulation to a single point projected onto the cortex, used a point-cloud to represent the TMS samples and derived the motor representation from it based on a fixed threshold. Operationalizing the similarity between TMS data and DCS data, has been done in a number of ways. For TMS this was done using either the location of the stimulus eliciting the largest MEPs (e.g. Forster et al., 2011; Tarapore et al., 2012), the location of the stimulus eliciting MEPs at the lowest stimulation intensity (e.g. Picht et al., 2009) or by calculating the center of gravity (CoG, i.e. the geometrical midpoint) of the thresholded outline (e.g. Takahashi et al., 2013; Zdunczyk et al., 2013). Average distance measures varied between studies from 2.1 mm (Tarapore et al., 2012) to 10 mm (Forster et al., 2011; Picht et al., 2009) and more, depending on the muscle of interest, and with a large range. More detailed maps of the motor representation can be obtained from this point-cloud by spline interpolation (Pitkänen et al., 2017). The thresholding is based on measured MEP-amplitudes known to show considerable trial-to-trial variability (Bastani and Jaberzadeh, 2012) and to be dependent on the relative orientation of the induced electrical field with respect to the underlying brain anatomy and properties of tissues underneath the TMS coil (Laakso et al., 2014; Thielscher et al., 2011). To improve the localization of the motor cortex, modelling of the induced electrical field might be useful, taking into account the coil properties, its orientation and the properties of different tissue classes that make up the inside of the head (Windhoff et al., 2013). Several algorithms have been published to calculate the induced electric field, e.g. the SimNibs workflow (Thielscher et al., 2015). In this study, we tested several ways of calculating the motor representation, with increasing complexity, and compared the maps with intraoperative DCS data of patients with Rolandic brain tumors. Our aim was to determine what model is best suited to determine the motor representation and to make suggestions to optimize TMS mapping data analysis for clinical practice.

2. Methods

2.1. Participants

Patients with tumors close to or extending into the motor cortex were prospectively invited to undergo TMS mapping prior to neurosurgery, between February 2014 and September 2016. Active epilepsy and treatment with anti-epileptic drugs (AEDs) was not a contra-indication for participation since the safety of TMS in this patient group has been documented to be comparable to healthy subjects (Pereira et al., 2016). A tailored craniotomy based on neuronavigation and fMRI data and intraoperative DCS were performed in all cases. The study was approved by the local Ethics Committee of the University Hospitals Leuven. All patients gave written informed consent.

2.2. Ground truth data: direct electrical cortical stimulation (DCS)

The neurosurgical team was blinded for the pre-operatively acquired TMS data until after the surgery. During the surgical intervention, DCS data were obtained with the purpose of determining a safe corticotomy. The points of DCS were recorded in the neuronavigation system for off-line analysis (BrainLab, Germany). The locations of the points sampled on the navigation scan were extracted with a research tool provided by BrainLab. Since the craniotomy often caused some brain deformation, resulting in small shifts of the cortical surface compared to preoperative images, the DCS points were projected onto the nearest point of the cortical surface in the pre-operative MR imaging (see below) prior to further analysis. To serve as ground truth for comparison with the TMS maps, a binary map of the motor representation was necessary. Hence a DCS stimulation resulting in a motor response at any given intensity was thus considered a positive DCS point and the other points as negative; nearest neighbor interpolation was used in order to obtain the binary map from those DCS points. Since no data could be obtained from non-exposed cortex using DCS, the ground truth map was limited to the exposed cortex (Fig. 1).

2.3. TMS mapping procedure

TMS data were acquired in the days prior to the surgery. During TMS data acquisition, patients were seated comfortably in a chair with a tracker placed on their head for online, non-invasive registration/reference of the head to an anatomical MRI scan. Stimulation was performed with a Magstim Rapid2 (Magstim, United Kingdom), with standard 70-mm figure-8 coil; neuronavigation data and EMG measurements were recorded using BrainSight (Rogue Research, Canada). EMG was measured using pre-gelled Ag/AgCl electrodes affixed in a belly-tendon montage over the muscles of interest, namely abductor pollicis brevis muscle (APB) for the upper limb and tibialis anterior muscle (TA) for the lower limb. Determination of the stimulation intensity was done in accordance to published guidelines (Groppa et al., 2012; Krieg et al., 2017) and set to 110% of the resting motor threshold of the muscle of interest and was kept constant during the procedure. Since MEPs have been shown to exhibit considerable trial-to-trial variability in amplitude (Bastani and Jaberzadeh, 2012) and the MEP amplitudes were used in further calculations, care was taken to obtain enough samples. This was done by sampling over a predetermined grid and taking 10 samples on each grid position. Mapping was continued in each direction until no MEP was seen in at least 5 consecutive measurements over the same grid position. Sampling was first performed over a 1x1cm grid and followed by sampling midway between those grid points. MEPs were measured as peak-to-peak amplitudes, of the maximal peak in the 10–90 ms time frame- trials with (voluntary) muscle activity prior to 10 ms were discarded.

2.4. Creation of the individual 3D head models

The anatomical T1- and T2-weighted images of the patients were used as input to generate a 3D volumetric mesh, consisting of different tissue classes, namely skin and subcutaneous tissue, skull, cerebrospinal fluid, grey matter, white matter, ventricles and brainstem with cerebellum, using surface and volume based meshing, as incorporated in the SimNibs workflow (Windhoff et al., 2013) (Fig. 2).

Tumor tissue was segmented manually and incorporated into the volumetric head model, taking care not to cause overlap with any of the other tissue classes. This was accomplished by manual segmentation in combination with meshing and mesh subtraction using VTK (ww.vtk.org) and correcting resulting meshes using meshfix (Attene, 2010).

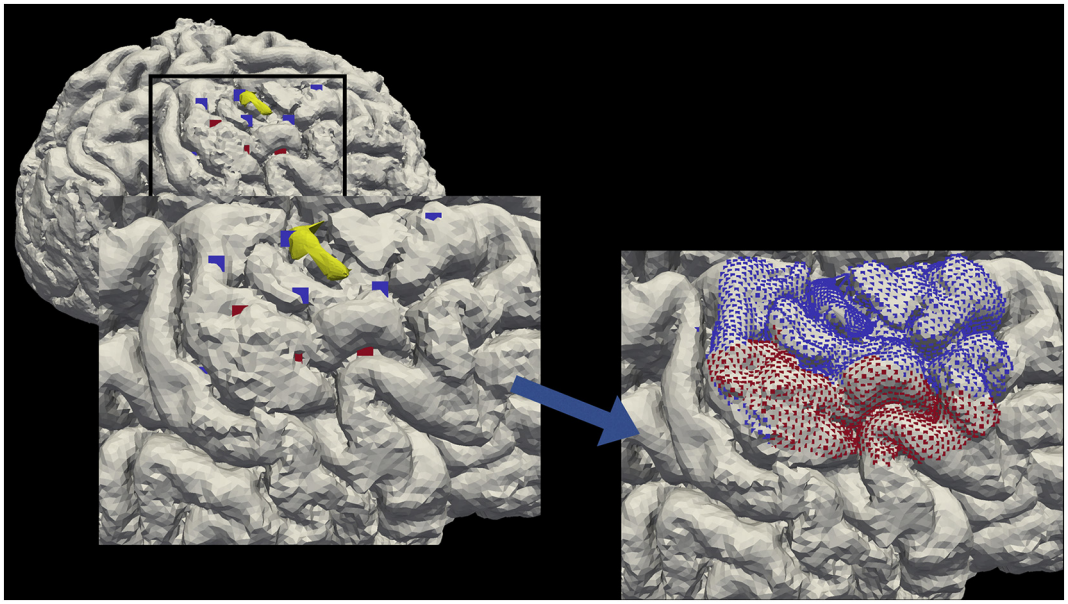

Fig. 1. Ground truth binary map derived from direct electrical cortical stimulation (DCS) data- for upper limb in this example.
DCS points are represented as squares on the cortical (or tumor = yellow) surface; blue squares: no motor response evoked (in this example in hand muscles) in this location; red squares: motor response evoked in hand muscles in this location, at any stimulation intensity.
A binary map of the exposed cortex was derived from these DCS-points, assigning either a positive or negative value to each node of the cortical surface map, based on the value of the nearest DCS point.

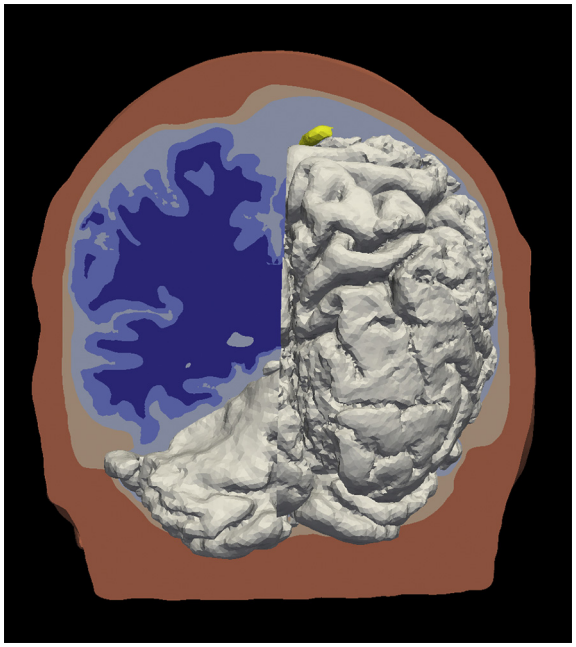

Fig. 2. Individual 3D head model based on anatomical MRI. 3D volumetric mesh-model of an individual subject; left: cut thought the different tissue classes: skin and subcutaneous tissue (pale red), skull (pale pink), cerebrospinal fluid (light blue), grey matter (light blue), white matter (dark blue); right: 3D surface of cortex (grey) and tumor (yellow).

2.5. Creation of the different probability maps

The workflow to create the different models from the TMS mapping data is illustrated in Fig. 3. The input data are the same for all models: the anatomical MRI and the coil positions and corresponding MEP amplitudes of all TMS-samples. Models can be divided into point-cloud based models (*method 1&2*), induced electric field based models (*method 4*) or a combination of both (*method 3*). Point-clouds were created by projecting the center of the TMS coil from the scalp to the cortical surface, for each sampled position, either to the nearest point (*method 1*) or along the plane perpendicular to the coil surface (*method 2*). From point-clouds a map was created using interpolation in order to obtain a model of the motor representation (Pitkänen et al., 2017). The electric field induced in the head by the magnetic field of the TMS coil was calculated for each patient and each coil position, based on SimNibs algorithms. We adapted those in order to retain the actual 3D position and orientation of the coil throughout the process to account for the varying coil-scalp distance as the strength of the induced field falls off with the inverse power of the distance, and to include a tumor. In the calculation of the induced field, each tissue class had different conductive properties. In a simpler model, all tissue conductivities were set as equal, which we will called “isotropic”; in “anisotropic” modelling each tissue class was assigned conductive properties based on literature data. In order not to bias the results, we set the conductive properties of the tumor to the same value as the grey matter. Since tumor is also rich in cell bodies, we assumed the conductivity to be most similar to this tissue class, although accurate data are lacking. In order to combine all field calculations of all samples, either the point of maximal field strength on the cortical surface was taken and the maxima of all samples combined into a point-cloud (*method 3*) or a weighted average of all induced fields was calculated, using the MEP amplitudes as weighting factor (*method 4*).

2.6. Outcome parameters

Maps created were visualized as 3D models. Our primary outcome parameter was how well the maps predicted the ground truth data, namely the binary DCS-based maps of the exposed cortex. The similarity of each probability map compared to the DCS-map was calculated for each individual patient, and plotted using receiver operating characteristic (ROC) curves in Matlab (Matworks, USA). ROC curves visualize sensitivity and specificity of the TMS-based map compared to the ground truth map, in a threshold-independent way, since all possible thresholds are analyzed. Paired *t*-tests were used to study differences in the sensitivity and specificity of the different models. Moreover, the maps were thresholded and the overall accuracy of the

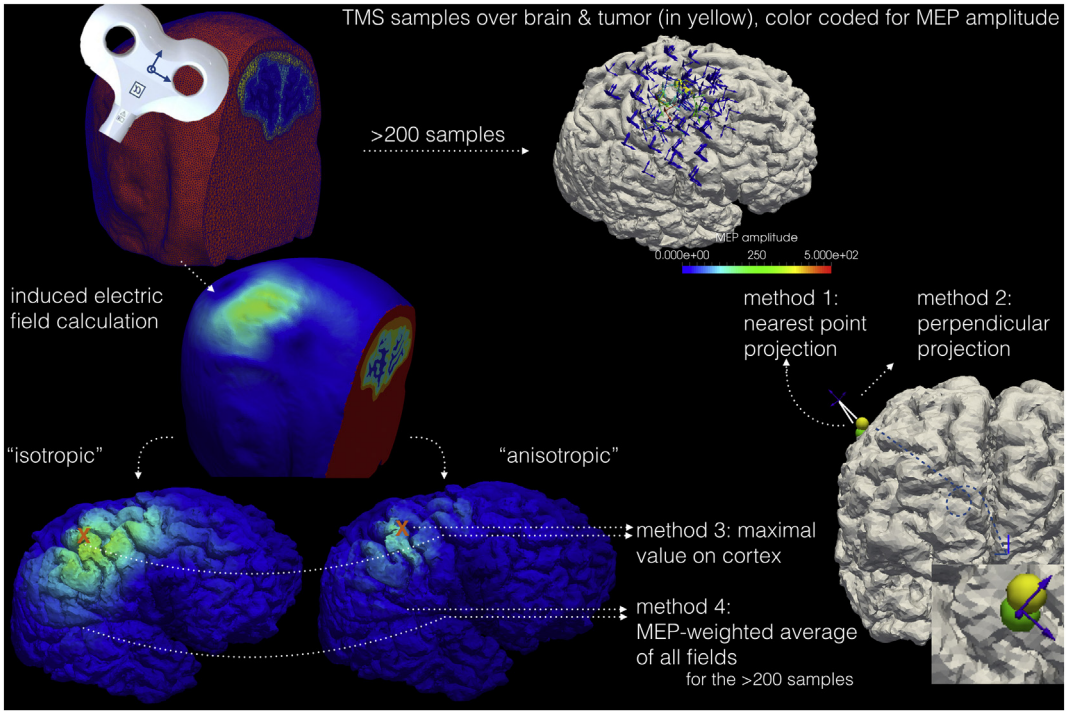

Fig. 3. Creation of the different probability maps. The position of the TMS coil in space is represented as a 3D Cartesian axis. Its location is reported relative to the position of the head of the subject. This was done by referencing the head of the subject to the anatomical MRI in a previous step and by using neuronavigation to track the TMS coil and the subjects' head. The anatomical MRI of the subject is converted into a realistic 3D model, to obtain a finite element model of the head, with its different tissue classes. All TMS samples are taken into account to generate the different models, together with their respective MEP amplitudes.
For method 3 and 4, the induced electric field was calculated for each coil position. This was done by either setting the conductive value of the different tissue classes to the same value, in the "isotropic" modelling, or by assigning realistic conductive properties to each tissue class, in the "anisotropic" modelling. Only the fields obtained in the cortex (and tumour surface) were used for further calculations. Method 3 used the maximal value of the induced field as point of activation, to obtain a map. In method 4 the whole field over the cortex was used and these were combined for the different samples, by obtaining a weighted average, with the MEP value as weighting factor.

different models was compared. Accuracy was defined as TP + TN/TP + TN + FP + FN (with TP: true positive, TN: true negative, FP: false positive and FN: false negative). These maps were also used to calculate centers of gravity (CoG) and compared to the location of the ground truth DCS points- CoG is the parameter used in most studies (the first study dating back to 1992 (Wassermann et al., 1992)). For point-cloud based maps, the threshold was set to 50 μV MEP-amplitude. In method 4, a fixed percentage of the maximal value was used as threshold (as suggested in Pitkänen et al., 2017) since the map is based on the strength of the induced field and not MEP-amplitudes.

3. Results

3.1. Participants and ground truth data: DCS

A flowchart of the patients screened and included can be found in Fig. 4. Patients' characteristics are given in Table 1. Twelve surgeries (one patient was operated twice) were included in our study. During neurosurgery, an average of eight (range: 5–11) locations were sampled with DCS. In eleven surgeries distal upper limb muscles were activated with an average of 2 (range: 1–3) positive responses per patient, and in three surgeries (including two that also mapped the upper limb) the distal lower limb was activated with DCS, with 1 positive response per patient.

3.2. TMS mapping procedure

For upper limb mapping, an average of 213 samples (± 76) were recorded in 11 patients and 142 samples (range: 120–185) for lower limb mapping in three patients (Table 1). The anatomical MRI used for

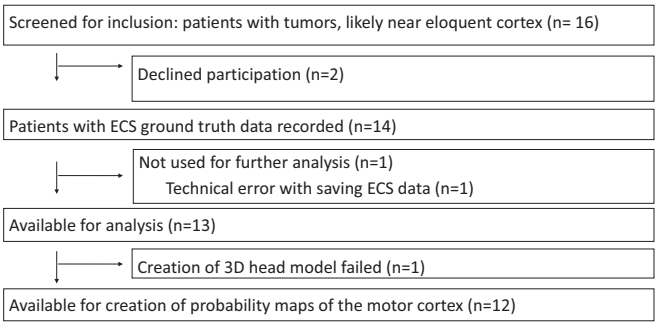

Fig. 4. Flowchart of recruitment and selection.

mapping and creation of the head models was recorded within a median of 17 days prior to surgery, with one outlier who underwent the fMRI 5 months prior to surgery (slow growing lesion).

3.3. Creation of the different probability maps

A representative example of one patient is shown in Fig. 5. Models 1–3 represent the location of motor areas, derived from the measured MEP amplitudes and scaled accordingly. Model 4, however, represents the areas where high induced electric fields are expected to generate MEPs.

3.4. Outcome parameters

The ROC curves of the models can be seen in Fig. 6. Since all point-

Table 1
Patients' characteristics.

	Age	Gender	Pathology	Relapse/ previous resection?	Prior seizures	AED type	AED dose	DCS positive distal upper limb/total	Number of TMS pulses for upper limb mapping[a]	DCS positive distal lower limb/total	Number of TMS pulses for lower limb mapping[a]
1	52	M	HGG WHO IV	N	Y	LEV/ VPA	2000/ 1500 mg	1/11	363	0/11	
2	19	F	LGG WHO II	N	N	–	–	2/8	100	0/8	
3	57	M	HGG WHO IV	Y	Y	LEV	1000 mg	1/5	268	0/5	
4	30	M	LLG WHO II	Y	Y	CBZ/ LEV/ VPA	600/1500/ 1750 mg	3/7	237	0/7	
5	46	M	LGG WHO II	N	N	–	–	1/10	170	0/10	
6	73	M	HGG WHO IV	Y	Y	LEV	2000 mg	3/7	119	0/7	
7	70	M	HGG WHO IV	Y	Y	LEV	1000 mg	1/8	195	0/8	
8	49	M	LGG WHO II	N	Y	LEV	1000 mg	1/8	280	0/8	
9	33	M	LCC, NOS	N	N	–	–	0/8		1/8	120
10[b]	56	M	HGG WHO IV	N	Y	LEV	2000 mg	5/9	258	1/9	120
11[b]	56	M	HGG WHO IV	Y	Y	LEV	2000 mg	3/8	175	1/8	185
12	71	F	metastatic RCC	N	N	–	–	2/7	180	0/7	

Abbreviations: AED: anti-epileptic drugs; CBZ: carbamazepine; LEV: levetiracetam; VPA: valproate; DCS positive upper/total: number of intra-operative positions sampled with DCS during surgery compared to the total number of samples acquired; DCS positive lower/total: same for lower limb responses; HGG: high grade glioma; LCC, NOS: large cell carcinoma, not otherwise specified: metastasis without known primary tumor; LGG: low grade glioma; RCC: renal cell carcinoma; Y: yes, N: no; WHO: world health organisation classification.

[a] data for mapping only reported if used in this study- that is, if intraoperatively the limb was also sampled.

[b] data are from the same patient, having two surgeries, 7 months apart.

based interpolated maps never covered the whole exposed cortex, the ROC curves of those models are truncated; the area-under-the-curve (AUC) parameter in those instances is not so meaningful. The average AUC parameter of model 4 isotropic was 79% (± 10%) and for the anisotropic model 75% (+/− 10%). The overall accuracy of model 1 was 86%, of model 2 85%, of model 3 isotropic 85%, of model 3 anisotropic 83%, of model 4 isotropic 64% and model 4 anisotropic 80%. Accuracies are driven primarily by the specificity due to the higher number of negative DCS points compared to positive points. Sensitivity and specificity of the different models, at optimal threshold, as based on the ROC curves, are found in Table 2. The best cut-off for model 4 isotropic was around 50% of the maximal value, as reported previously (Pitkänen et al., 2017) whereas for the anisotropic model, a cut-off of around 40% of maximal (cut-offs were tested with 10% increments (Pitkänen et al., 2017)), performed better - the maximal value obtained with the anisotropic models was on average also 14% higher compared to the isotropic model. 50% and 40% cut-offs respectively were thus used to threshold the map for CoG calculations. However, accuracies of the models at the fixed threshold were similar to the accuracy data obtained from the ROC curves (Table 3). The Euclidian distance between the CoG of a model and the DCS point is on average 11 mm (SD 1.5 mm) (Tables 4a, 4b). For the six subjects in whom more than one positive DCS point was recorded, the distance measures decreased for the electric field based models when the DCS point was taken where a response could be evoked with the lowest amount of stimulating current instead of the center of the DCS points (table 5); however this difference was not significant in this low number of subjects.

4. Discussion

TMS is a useful and accepted method to locate the motor cortex prior to neurosurgical procedures. Its accuracy depends on the ability to predict from the position of the coil (with a coil diameter spanning over ten centimeters) placed on the head, the area of activation in the cortex. TMS does affect a whole area of the brain, rather than a single “activation point” as it has often been presented in previous studies. In this study, we created probability maps of the motor cortex that differed only in the way they were calculated, by adding progressively more information. The electric fields were calculated post-hoc from the scalp location- not during the recording- and thus more detailed and computationally complex methods could be used. The modelling could not only take scalp- brain distance and properties of the magnetic coil into account, but all anatomical details of the individual's head and the differential conductive properties of tissue classes. The aim was to determine the best way to analyze the TMS data in order to delineate the cortical motor representation, i.e. the cortical area that is necessary and sufficient for motor function. It was shown that simple projection models are accurate (accuracy ≥85%) and can be used to specifically point to a cortical area of the motor cortex (specificity > 95%). However, the spread of activation is not captured. Clinically, these models can be used to pinpoint to a gyrus containing the motor cortex. Using the induced field to determine the point of maximal impact in the brain of the TMS pulse, did not improve the model compared to simple projections. The modelling did not only take scalp-brain distance and properties of the magnetic coil into account, but also all anatomical details of the subjects' head. In this modelling, the anisotropic model showed often only a very small area of activation; due the inherent local field increases at grey-white matter borders (Thielscher et al., 2011) the maxima of samples obtained over larger areas of the scalp coincided on the same focal point at a bend of a sulcal surface. The reason for this lack of additional benefit is that the effect of TMS is more extensive than one focal point- a fact we wanted to capture in the electric field weighted average models. The interpretation of those maps is that regions with high values are those where high induced electric field strengths are likely to result in high MEP amplitudes. These maps can give an outline of the motor were 50% of the maximal value for the isotropic and 40% for the anisotropic model.

For clinical purposes, we suggest to use different thresholds, which is a unique benefit of these maps: a high threshold highlights the center of the motor area and a lower threshold is able to capture the whole motor representation (Fig. 7). The best accuracy for this type of probability map was obtained by the anisotropic version of this model, which the model that takes all known information of anatomy and conductivity into account.

In order for these models to work, care needs to be taken to counter the inherent considerable trial-to-trial variability in MEP amplitudes, for instance by measuring several MEP amplitudes from a similar location and by using an interpolation over the surface, which should limit problems caused by outliers (Pitkänen et al., 2017), as was done in our study. It should be noted that previous motor TMS studies in

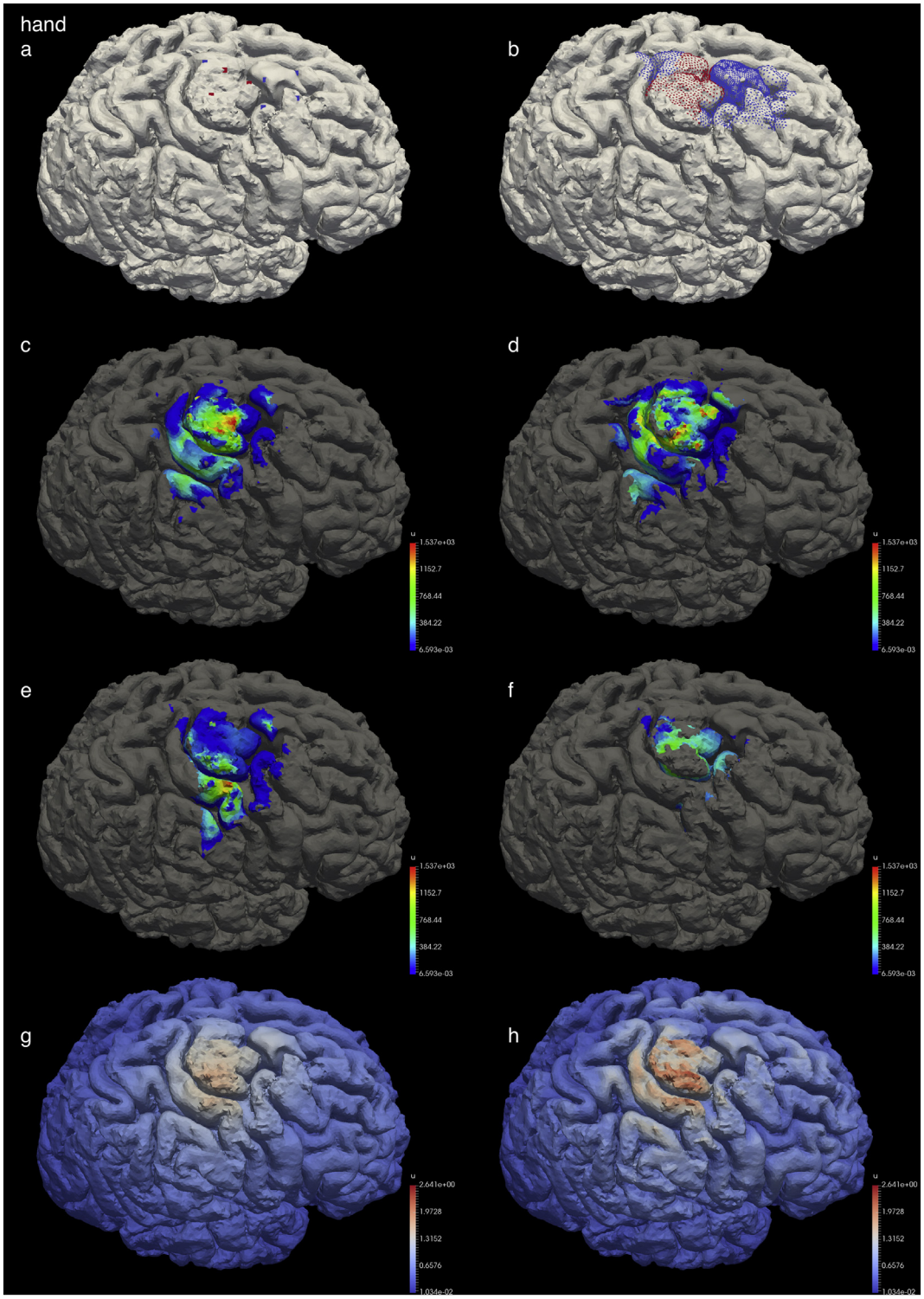

Fig. 5. All models for one patient in the study, both for upper and lower limb panel a: DCS points sampled during surgery; panel b: ground truth map (similar to Figure 1) panel c: method 1: based on nearest-point projection, with interpolation over the surface, color coding refers to measured MEP amplitudes (in μV) panel d: method 2: based on projection along a plane perpendicular to the coil, with interpolation over the surface, color coding refers to measured MEP amplitudes (in μV) panel e: method 3 isotropic: based on the maximum of the induced field of each coil position sampled, color coding refers to measured MEP amplitudes (in μV) panel f: method 3 anisotropic: same as panel e but using tissue-specific conductivity values based on known tissue properties panel g: method 4 isotropic: based on MEP-amplitude informed weighted average of all fields, color coded for where high induced fields are likely to result in high MEP-amplitudes (red) and areas of low probability of motor responses (blue)panel h: method 4 anisotropic: same as panel g but using a tissue-specific conductivity value based on known tissue properties.

neurosurgical patients used a simple curvilinear representation of the cortical surface whereas we used the real cortical surface. This inherently leads to larger Euclidian differences between two points and distance measures. Our results, therefore, are not completely comparable with previous studies. Moreover, the CoG is dependent on the cut-off used and especially for field-based models; the CoG shifts considerably when changing the threshold and is thus not a robust outcome measure. The average distance in our study was 11 mm,

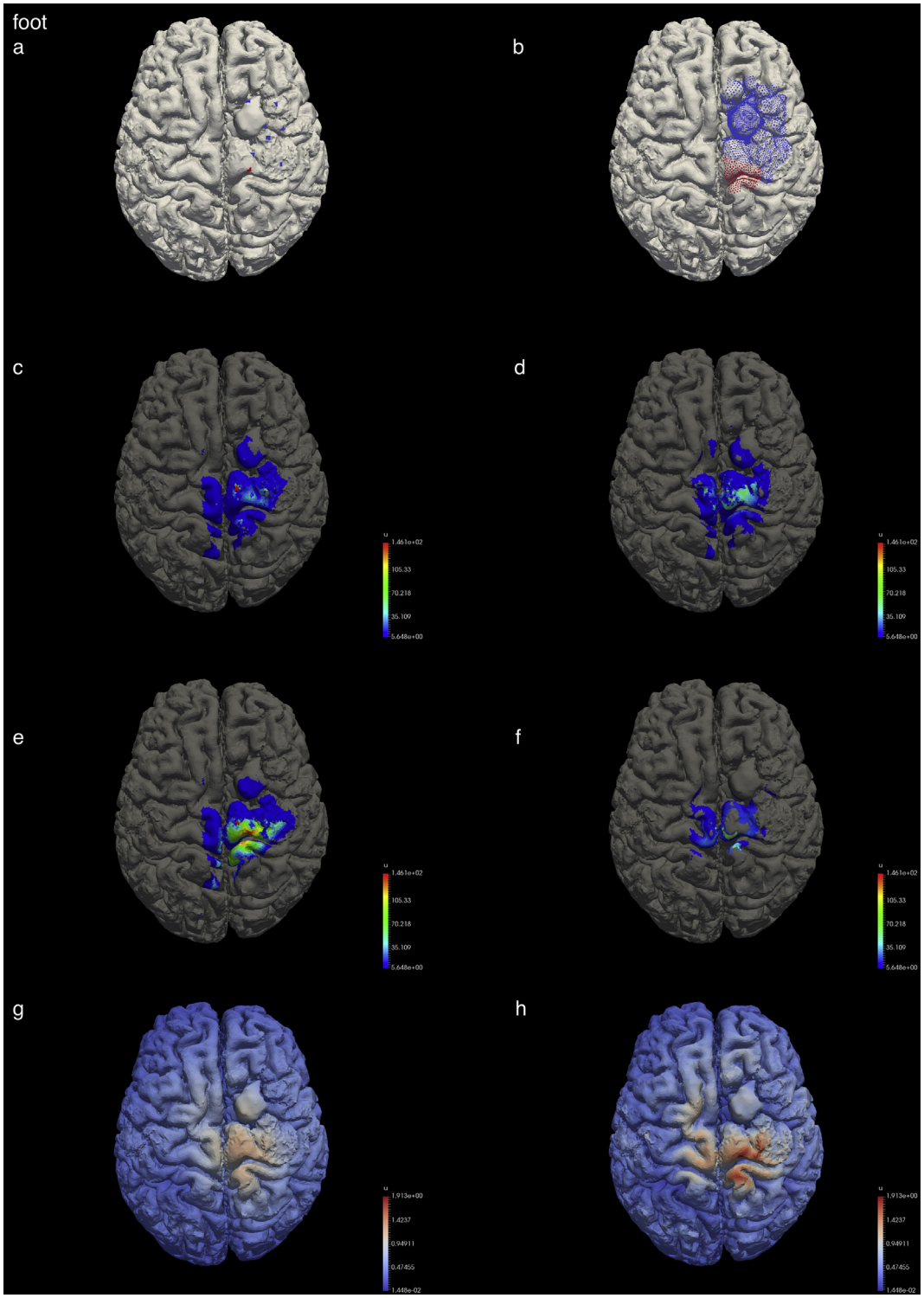

Fig. 5. (*continued*)

depending on the modelling used. The rather low number of DCS points in our study also affected distance measures, but the resulting ground truth map was clinically relevant. It was left to the discretion of the neurosurgeon (who was blinded for the pre-operatively acquired TMS results) to determine the location and number of DCS points, which in this study were based mainly on sulcal anatomy. Previous studies have used a setup were the TMS-based locations of the motor cortex have been used to guide the DCS sampling (Finke et al., 2008; Kantelhardt et al., 2010; Mangraviti et al., 2013; Picht et al., 2009) or have used a much higher number of DCS points (Picht et al., 2011), both of which can improve distance measures. The ground truth data in our study also did not have any information on contribution of different parts within one gyrus to the resulting motor output, since this was not the aim of the study. The anisotropic induced field based model predicts that different parts of one gyrus contributing unequally to the resulting motor output. Whether this can also be demonstrated using DCS mapping, will need further study. It should also be noted that the modelling in this study was based on priors derived from healthy volunteers. The model could benefit from more knowledge about the differential conductivity of (different parts of) the tumor, especially if it was combined

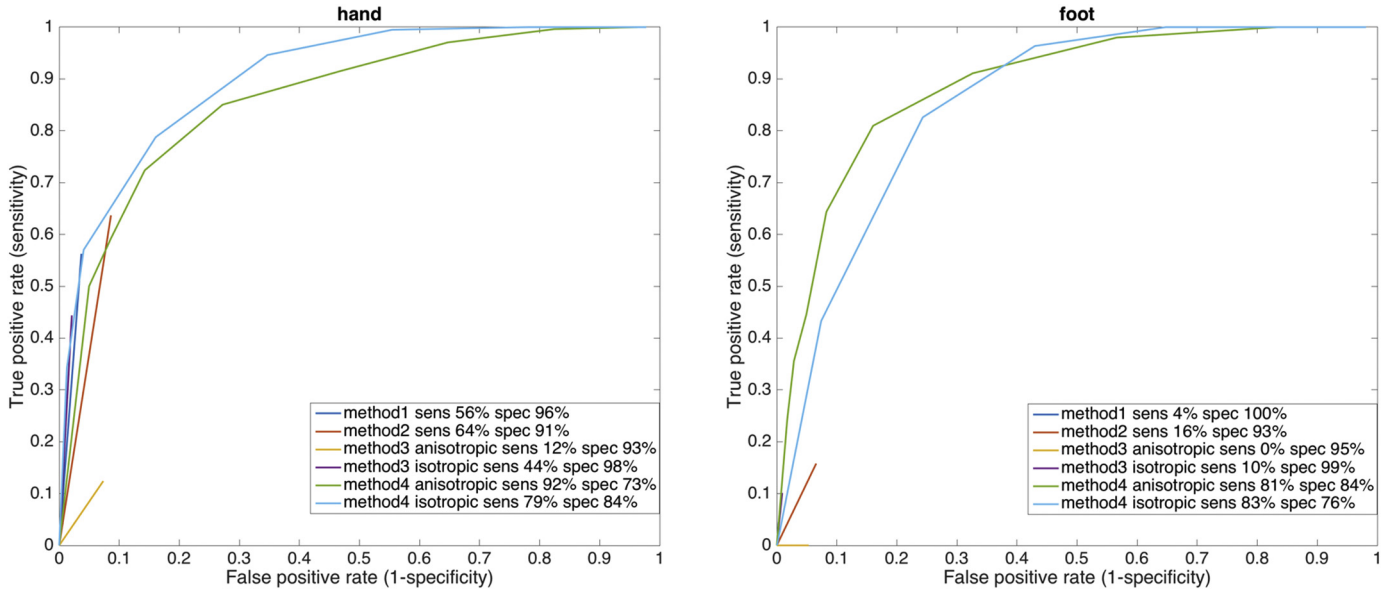

Fig. 6. Receiver-operator characteristics (ROC) curves of the experimental maps of the subject who's maps are represented visually in Figure 5. Since the point-based methods do not have values for all points of the cortical (and tumour) surface, those graphs are truncated. Sensitivity and specific values are reported for the optimal cut-off. The area under the curse (AUC) for hand is 0.88 for the isotropic method and 0.83 for the anisotropic method; for the foot this is 0.84 and 0.86 respectively.

Table 2
Sensitivity and specificity of the different models (in %), for the different patients, compared to the DCS data, as calculated from the ROC curves.

	Method 1		Method 2		Method 3 isotropic		Method 3 anisotropic		Method 4 isotropic		Method 4 anisotropic	
	Sens	Spec	Sens	Spec	Sens	Spec	Sens	Spec	Sens	Spec	Sens	Spec
Patient 1 hand	31	94	37	91	20	95	37	93	87	86	81	80
Patient 2 hand	77	56	67	89	51	94	61	88	100	47	96	55
Patient 3 hand	33	70	68	68	7	75	3	90	85	48	76	58
Patient 4 hand	60	86	47	62	58	90	54	61	78	57	75	70
Patient 5 hand	28	98	33	97	39	96	53	91	80	81	65	74
Patient 6 hand	33	98	39	95	23	99	57	90	79	74	62	87
Patient 7 hand	32	87	48	87	19	78	10	100	71	72	67	60
Patient 8 hand	50	81	71	87	57	76	90	53	77	70	74	66
Patient 9 foot	68	87	82	83	36	92	79	77	94	72	74	79
Patient 10 hand	56	96	64	91	44	98	12	93	79	84	92	73
Patient 10 foot	4	100	16	93	10	99	1	99	83	76	81	84
Patient 11 hand	28	90	73	77	28	88	15	96	60	55	45	57
Patient 11 foot	97	85	94	85	97	86	47	93	96	84	93	96
Patient 12 hand	49	78	44	82	48	76	44	76	96	28	89	49
Mean (+standard deviation)	46,1 (27,9)	86,1 (7,3)	55,9 (24,7)	84,8 (5,1)	38,3 (23,9)	88,7 (9,4)	40,2 (33,5)	85,7 (16,2)	83,2 (13,0)	66,7 (18,4)	76,4 (16,0)	70,6 (15,5)

Table 3
accuracy (in %) of the different thresholded maps, for the different patients, compared to the DCS based map ('ground truth').

Accuracy thresholded		Model 1	Model 2	Model 3 isotropic	Model 3 anisotropic	Model 4 isotropic	Model 4 anisotropic
Patient 1 Hand		89	90	85	90	90	86
Patient 2 Hand		82	87	84	86	81	74
Patient 3 Hand		95	83	81	85	84	68
Patient 4 Hand		85	70	73	88	84	45
Patient 5 Hand		94	94	89	94	93	80
Patient 6 Hand		50	54	53	42	62	76
Patient 7 Hand		88	89	88	88	45	53
Patient 8 Hand		87	90	88	86	81	71
Patient 9 Foot		87	85	78	86	82	63
Patient 10 Hand		78	82	77	78	85	66
Patient 10 Foot		93	93	93	93	92	41
Patient 11 Hand		77	80	76	75	78	61
Patient 11 Foot		95	95	95	98	96	62
Patient 12 Hand		85	85	85	85	45	47
Total	All: mean & stand-dev	85 (12)	84 (11)	82 (11)	84 (14)	78 (16)	64 (14)
	Hand: mean & stand-dev	83 (12)	67 (11)	65 (10)	66 (14)	60 (17)	53 (14)
	Foot: mean & stand-dev	91 (4)	91 (5)	88 (10)	92 (6)	90 (7)	55 (12)

Table 4a
Distances (in mm) of the centre of gravity (CoG), using pre-set thresholds, between each of the models and the positive DCS point (single positive DCS point (in 6/12) when only one positive DCS point was recorded or to the midpoint of all positive DCS points (marked with *)).

	Method 1	Method 2	Method 3 isotropic	Method 3 anisotropic	Method 4 isotropic	Method 4 anisotropic
1 Hand	17.9	18.5	15.0	17.7	22.1	25.4
2* Hand	12.9	12.1	10.0	10.6	18.0	18.7
3 Hand	21.2	18.7	24.2	24.2	35.8	37.8
4* Hand	9.2	8.4	11.1	5.4	12.3	11.8
5 Hand	16.6	18.3	14.3	16.1	21.4	23.0
6* Hand	8.3	10.6	16.4	14.6	18.6	18.9
7 Hand	13.1	7.1	9.2	19.1	11.0	14.3
8 Hand	11.9	13.7	13.2	9.0	13.0	12.6
9 Foot	7.7	9.0	6.3	6.5	9.1	11.7
10* Hand	10.4	6.9	10.1	10.3	9.9	12.0
10 Foot	NaN	17.5	11.0	NaN	13.2	20.9
11* Hand	17.0	11.4	12.8	12.0	19.1	20.5
11 Foot	5.9	5.9	8.2	6.1	14.0	18.0
12* Hand	4.9	4.0	NaN	NaN	11.3	14.4
All mean (standard dev)	12.7 (5.0)	11.3 (5.1)	11.5 (4.5)	10.8 (5.8)	16.7 (7.0)	17.5 (7.1)
Hand mean (standard dev)	13.0 (4.8)	11.8 (5.1)	13.6 (4.4)	13.9 (5.5)	17.5 (7.5)	19.0 (7.7)
Foot mean (standard dev)	4.5 (1.3)	8.1 (6.0)	6.4 (2.4)	4.2 (0.3)	9.1 (2.6)	12.7 (4.7)

with automated and reliable tumor segmentation. Moreover, TMS based mapping cannot sample selectively from subcortical structures and thus in order to preserve white matter tracts during surgery, another mapping technique will need to be added (like tractography or intraoperative direct subcortical stimulation).

Depending on the clinical question, a different way to analyze the motor TMS data can be chosen. We argue that calculating a realistic head model and obtaining a weighted average electric field based model, is preferable, since it captures more information compared to point-cloud based models is feasible since it is based on data available preoperatively and a workflow with freely available software. The input data can be acquired with a number of different TMS equipment (including coils from different vendors) and software. It is also more robust since the model takes the coil orientation into account and averages out the inherent MEP-amplitude variability. Since acquisition can be done separately from analysis, pooling of data from different centers becomes a possibility and could be exploited to explore the modelling's full potential. The output is an easy to manipulate, threshold-adjustable detailed 3D model of the patients' brain, which can be loaded in the intraoperative navigation software.

Table 5
Distances (in mm) for the ground truth maps: between DCS mean- that is the midpoint of all positive DCS points or a single positive DCS point (in 6/12) when only one positive DCS point was recorded DCS single- the single DCS point where the response was evoked at the lowest stimulation intensity (if available) and the CoG of the DCS positive maps created by nearest neighbor interpolation.

	DCS single-DCS mean	CoG-DCS mean	CoG-DCS single
Patient 1 hand	–	8.6	–
Patient 2 hand	8.6	5.5	12.9
Patient 3 hand	–	8.8	–
Patient 4 hand	11.4	6.0	10.0
Patient 5 hand	–	9.4	–
Patient 6 hand	12.8	17.9	12.6
Patient 7 hand	–	3.7	–
Patient 8 hand	–	5.4	–
Patient 9 foot	–	6.5	–
Patient 10 hand	13.8	6.2	7.7
Patient 10 foot	–	2.7	–
Patient 11 hand	16.9	11.3	18.0
Patient 11 foot	–	4.5	–
Patient 12 hand	12.8	10.2	5.1
Mean	12.7	7.6	11.1
Standard deviation	2.7	3.9	4.5

Disclosure

This work was supported by the Institute for innovation by science and technology Flanders (IWT) [TBM grant 09085].

Acknowledgments

The work has been awarded a Belgian Brain Tumor Support prize in 2016.

We would like to thank the patients and their caregivers for participation in the trial, the colleagues of the department of Neurology and Neurosurgery for their organizational support, special thanks goes to Mr. Van Driel for the intra-operative data collection, to the Medical Imaging Research Centre colleagues for technical support and to Dr. Duerinck for the critical revision of a previous version of this manuscript.

Appendix A. Supplementary data

Supplementary data to this article can be found online at https://

Table 4b
Distances (in mm) of the centre of gravity (CoG), using pre-set thresholds, between each of the models and the single DCS point where a response was evoked using the lowest current, in patients with more than one DCS positive point recorded (in all for mapping of the hand).

	Method 1	Method 2	Method 3 isotropic	Method 3 anisotropic	Method 4 isotropic	Method 4 anisotropic
2	6.5	6.3	7.1	8.9	9.9	9.1
4	2.9	6.7	8.8	10.6	13.0	9.0
6	6.8	8.5	9.4	11.5	12.2	12.2
10	6.5	6.5	6.5	10.2	14.6	9.0
11	24.0	22.4	13.7	12.1	3.8	1.9
12	4.6	1.7	7.2	7.2	7.3	8.3
Mean (Stand dev)	8.6 (7.7)	8.7 (7.1)	8.8 (2.6)	10.1 (1.8)	10.1 (4.0)	8.3 (3.4)

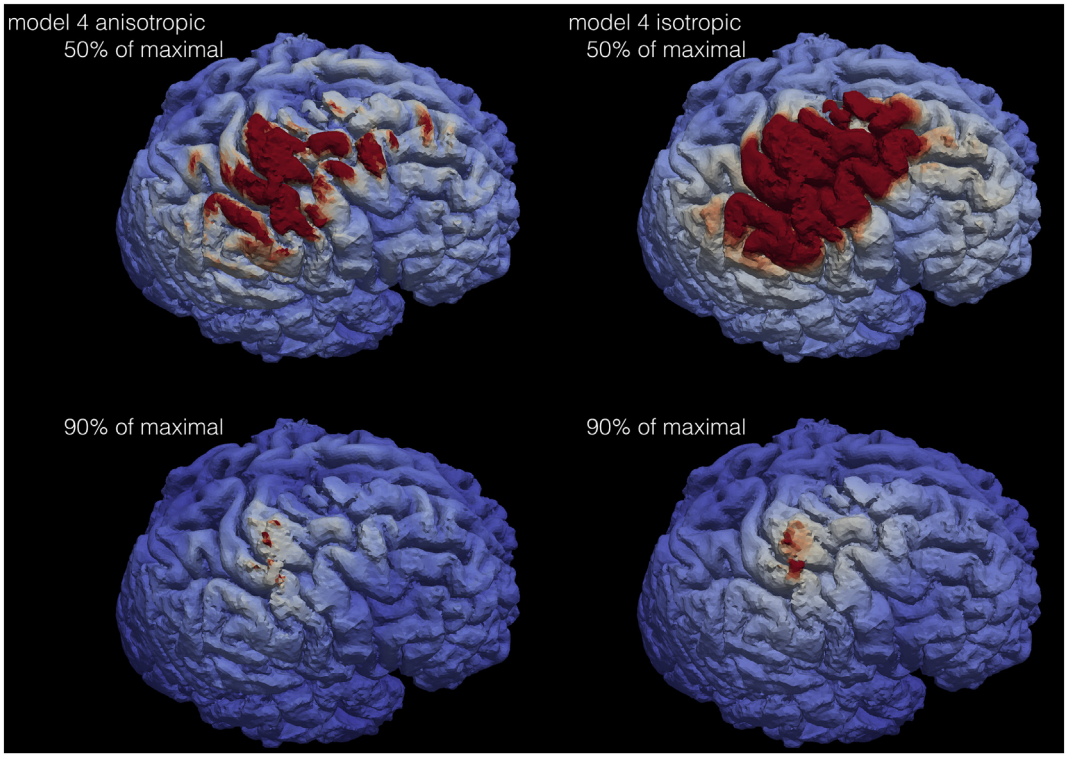

Fig. 7. Illustration of the effect of the chosen threshold on the corresponding map. The upper and lower panels represent the same map, but at a different threshold, to demonstrate that with the same map both the area of the motor representation can be shown (although at the cost of some false-positive zones) and the motor "hotspot". This image also illustrates that the anisotropic map is often more suited to gauge the motor representation.

doi.org/10.1016/j.nicl.2019.101657.

References

Attene, M., 2010. A lightweight approach to repairing digitized polygon meshes. Vis. Comput. 26, 1393–1406. https://doi.org/10.1007/s00371-010-0416-3.

Bastani, A., Jaberzadeh, S., 2012. A higher number of TMS-elicited MEP from a combined hotspot improves intra- and inter-session reliability of the upper limb muscles in healthy individuals. PLoS One 7. https://doi.org/10.1371/journal.pone.0047582.

Finke, M., Fadini, T., Kantelhardt, S., Giese, A., Matthaus, L., Schweikard, A., 2008. Brain-mapping using robotized TMS. In: Conf. Proc. IEEE Eng. Med. Biol. Soc. 2008, pp. 3929–3932. https://doi.org/10.1109/IEMBS.2008.4650069.

Forster, M.T., Hattingen, E., Senft, C., Gasser, T., Seifert, V., Szelényi, A., 2011. Navigated transcranial magnetic stimulation and functional magnetic resonance imaging: advanced adjuncts in preoperative planning for central region tumors. Neurosurgery 68, 1317–1324. https://doi.org/10.1227/NEU.0b013e31820b528c.

Groppa, S., Oliviero, a., Eisen, a., Quartarone, a., Cohen, L.G., Mall, V., Kaelin-Lang, a., Mima, T., Rossi, S., Thickbroom, G.W., Rossini, P.M., Ziemann, U., Valls-Solé, J., Siebner, H.R., 2012. A practical guide to diagnostic transcranial magnetic stimulation: report of an IFCN committee. Clin. Neurophysiol. 123, 858–882. https://doi.org/10.1016/j.clinph.2012.01.010.

Hill, D.L., Smith, A.D., Simmons, A., Maurer, C.R., Cox, T.C., Elwes, R., Brammer, M., Hawkes, D.J., Polkey, C.E., 2000. Sources of error in comparing functional magnetic resonance imaging and invasive electrophysiological recordings. J. Neurosurg. 93, 214–223. https://doi.org/10.3171/jns.2000.93.2.0214.

Hou, B.L., Bradbury, M., Peck, K.K., Petrovich, N.M., Gutin, P.H., Holodny, A.I., 2006. Effect of brain tumor neovasculature defined by rCBV on BOLD fMRI activation volume in the primary motor cortex. NeuroImage 32, 489–497. https://doi.org/10.1016/j.neuroimage.2006.04.188.

Kantelhardt, S.R., Fadini, T., Finke, M., Kallenberg, K., Siemerkus, J., Bockermann, V., Matthaeus, L., Paulus, W., Schweikard, A., Rohde, V., Giese, A., 2010. Robot-assisted image-guided transcranial magnetic stimulation for somatotopic mapping of the motor cortex: a clinical pilot study. Acta Neurochir. 152, 333–343. https://doi.org/10.1007/s00701-009-0565-1.

Krieg, S.M., Lioumis, P., Mäkelä, J.P., Wilenius, J., Karhu, J., Hannula, H., Savolainen, P., Lucas, C.W., Seidel, K., Laakso, A., Islam, M., Vaalto, S., Lehtinen, H., Vitikainen, A.-M., Tarapore, P.E., Picht, T., 2017. Protocol for motor and language mapping by navigated TMS in patients and healthy volunteers; workshop report. Acta Neurochir. 159, 1187–1195. https://doi.org/10.1007/s00701-017-3187-z.

Krings, T., Buchbinder, B.R., Butler, W.E., Chiappa, K.H., Jiang, H.J., Cosgrove, G.R., Rosen, B.R., 1997. Functional magnetic resonance imaging and transcranial magnetic stimulation: complementary approaches in the evaluation of cortical motor function. Neurology 48, 1406–1416. https://doi.org/10.1212/WNL.48.5.1406.

Laakso, I., Hirata, A., Ugawa, Y., 2014. Effects of coil orientation on the electric field induced by TMS over the hand motor area. Phys. Med. Biol. 59, 203–218. https://doi.org/10.1088/0031-9155/59/1/203.

Mangraviti, A., Casali, C., Cordella, R., Legnani, F.G., Mattei, L., Prada, F., Saladino, A., Contarino, V.E., Perin, A., DiMeco, F., 2013. Practical assessment of preoperative functional mapping techniques: navigated transcranial magnetic stimulation and functional magnetic resonance imaging. Neurol. Sci. 34, 1551–1557. https://doi.org/10.1007/s10072-012-1283-7.

Pereira, L.S., Müller, V.T., da Mota Gomes, M., Rotenberg, A., Fregni, F., 2016. Safety of repetitive transcranial magnetic stimulation in patients with epilepsy: a systematic review. Epilepsy Behav. 57, 167–176. https://doi.org/10.1016/j.yebeh.2016.01.015.

Picht, T., Mularski, S., Kuehn, B., Vajkoczy, P., Kombos, T., Suess, O., 2009. Navigated transcranial magnetic stimulation for preoperative functional diagnostics in brain tumor surgery. Neurosurgery 65, 93–99. https://doi.org/10.1227/01.NEU.0000348009.22750.59.

Picht, T., Schmidt, S., Brandt, S., Frey, D., Hannula, H., Neuvonen, T., Karhu, J., Vajkoczy, P., Suess, O., 2011. Preoperative functional mapping for rolandic brain tumor surgery: comparison of navigated transcranial magnetic stimulation to direct cortical stimulation. Neurosurgery 69, 581–588. https://doi.org/10.1227/NEU.0b013e3182181b89.

Pitkänen, M., Kallioniemi, E., Julkunen, P., Nazarova, M., Nieminen, J.O., Ilmoniemi, R.J., 2017. Minimum-norm estimation of motor representations in navigated TMS mappings. Brain Topogr. 30, 711–722. https://doi.org/10.1007/s10548-017-0577-8.

Sunaert, S., 2006. Presurgical planning for tumor resectioning. J. Magn. Reson. Imaging 23, 887–905. https://doi.org/10.1002/jmri.20582.

Takahashi, S., Vajkoczy, P., Picht, T., 2013. Navigated transcranial magnetic stimulation for mapping the motor cortex in patients with rolandic brain tumors. Neurosurg. Focus. 34, E3. https://doi.org/10.3171/2013.1.FOCUS133.

Tarapore, P.E., Tate, M.C., Findlay, A.M., Honma, S.M., Mizuiri, D., Berger, M.S., Nagarajan, S.S., 2012. Preoperative multimodal motor mapping: a comparison of magnetoencephalography imaging, navigated transcranial magnetic stimulation, and direct cortical stimulation. J. Neurosurg. 117, 354–362. https://doi.org/10.3171/2012.5.JNS112124.

Thielscher, A., Opitz, A., Windhoff, M., 2011. Impact of the gyral geometry on the electric field induced by transcranial magnetic stimulation. NeuroImage 54, 234–243. https://doi.org/10.1016/j.neuroimage.2010.07.061.

Thielscher, A., Antunes, A., Saturnino, G.B., 2015. Field modeling for transcranial magnetic stimulation: a useful tool to understand the physiological effects of TMS? In: Conf. Proc. … Annu. Int. Conf. IEEE Eng. Med. Biol. Soc. IEEE Eng. Med. Biol. Soc. Annu. Conf. 2015, pp. 222–225. https://doi.org/10.1109/EMBC.2015.7318340.

Wang, L., Chen, D., Olson, J., Ali, S., Fan, T., Mao, H., 2012. Re-examine tumor-induced alterations in hemodynamic responses of BOLD fMRI: implications in presurgical brain mapping. Acta Radiol. 53, 802–811. https://doi.org/10.1258/ar.2012.120118.

Wassermann, E.M., McShane, L.M., Hallett, M., Cohen, L.G., 1992. Noninvasive mapping

of muscle representations in human motor cortex. Electroencephalogr. Clin. Neurophysiol. 85, 1–8.
Windhoff, M., Opitz, A., Thielscher, A., 2013. Electric field calculations in brain stimulation based on finite elements: an optimized processing pipeline for the generation and usage of accurate individual head models. Hum. Brain Mapp. 34, 923–935. https://doi.org/10.1002/hbm.21479.
Zacà, D., Jovicich, J., Nadar, S.R., Voyvodic, J.T., Pillai, J.J., 2014. Cerebrovascular reactivity mapping in patients with low grade gliomas undergoing presurgical sensorimotor mapping with BOLD fMRI. J. Magn. Reson. Imaging 40, 383–390. https://doi.org/10.1002/jmri.24406.
Zdunczyk, A., Fleischmann, R., Schulz, J., Vajkoczy, P., Picht, T., 2013. The reliability of topographic measurements from navigated transcranial magnetic stimulation in healthy volunteers and tumor patients. Acta Neurochir. 155, 1309–1317. https://doi.org/10.1007/s00701-013-1665-5.